

# Absolute Quantification of Myocardial Blood Flow with $H_2^{15}O$ and 3-Dimensional PET: An Experimental Validation

Klaus P. Schäfers, PhD<sup>1,2</sup>; Terence J. Spinks, PhD<sup>3</sup>; Paolo G. Camici, MD<sup>1</sup>; Peter M. Bloomfield, MSc<sup>3</sup>; Christopher G. Rhodes, DSc<sup>3</sup>; Marilyn P. Law, PhD<sup>1</sup>; Christopher S.R. Baker, PhD<sup>1</sup>; and Ornella Rimoldi, MD<sup>1</sup>

<sup>1</sup>Medical Research Council Clinical Sciences Centre and National Heart and Lung Institute, Faculty of Medicine, Imperial College of Science, Technology and Medicine, Hammersmith Hospital, London, United Kingdom; <sup>2</sup>Department of Nuclear Medicine, University of Münster, Münster, Germany; and <sup>3</sup>Imaging Research Solutions Ltd., Hammersmith Hospital, London, United Kingdom

The purpose of this study was to assess a 3-dimensional (3D)-only PET scanner (ECAT EXACT3D) for its use in the absolute quantification of myocardial blood flow (MBF) using  $H_2^{15}O$ . **Methods:** Nine large white pigs were scanned with  $H_2^{15}O$  and  $C^{15}O$  before and after partially occluding the circumflex ( $n = 4$ ) or the left anterior descending ( $n = 5$ ) coronary artery at rest and during hyperemia induced by intravenous dipyridamole. Radioactive microspheres labeled with either  $^{57}Co$  or  $^{46}Sc$  were injected during each of the  $H_2^{15}O$  scans, which allowed comparison between microsphere and PET measurements of regional MBF. PET analyses of 3D acquisition data were performed using filtered backprojection reconstruction and region-of-interest definition by factor and cluster analysis techniques and single-compartment model quantification. **Results:** The Hanning filter applied in image reconstruction resulted in a left atrial blood volume recovery factor of  $0.84 \pm 0.06$ . Differences between repeated measurements of recovery were small (mean,  $-0.8\%$ ; range,  $-6.6\%$  to  $3.6\%$ ). In 256 paired measurements of MBF ranging from  $0.05$  to  $4.4 \text{ mL} \cdot \text{g}^{-1} \cdot \text{min}^{-1}$ , microsphere and PET measurements were fairly well correlated. The mean difference between the 2 methods was  $-0.11 \text{ mL} \cdot \text{g}^{-1} \cdot \text{min}^{-1}$  and the limits of agreement ( $+2 \text{ SD}$ ) were  $-0.82$  and  $0.60 \text{ mL} \cdot \text{g}^{-1} \cdot \text{min}^{-1}$  (Bland-Altman plot). **Conclusion:** Dynamic measurements with  $H_2^{15}O$  using a 3D-only PET tomograph provide reliable and accurate measurements of absolute regional MBF over a wide flow range. The 3D acquisition technique can reduce the radiation dose to the subject while maintaining adequate counting statistics.

**Key Words:** myocardial blood flow; 3-dimensional PET; absolute quantification;  $H_2^{15}O$

**J Nucl Med 2002; 43:1031-1040**

At present, PET is the only technique that can provide noninvasive absolute quantification of regional myocardial blood flow (MBF) in humans. Using  $H_2^{15}O$ , we have shown recently that MBF and coronary vasodilator reserve can be measured with PET (1) with good reproducibility. The application of perfusion studies to cardiology has allowed the investigation of the functional significance of coronary stenoses (2,3) as well as the assessment of the function of the coronary microvasculature (4). The PET cameras used previously for the quantification of MBF, as well as for other cardiac applications of PET, work in the 2-dimensional (2D) mode with collimating septa between the detector rings to reduce the number of interplane scattered photons (5). However, more recently, a new generation of 3-dimensional (3D)-only tomographs has become available with potential benefits over 2D systems (6). The main advantage of data acquisition in the 3D mode is the high sensitivity to better exploit the intrinsic spatial resolution and the lower radiation dose to patients. In the 3D mode, the scatter fraction is higher and, for a given administered dose, the randoms fraction is higher than that in the 2D mode, which implies that correction methods need to be more accurate. However, because of the higher 3D efficiency, it has been shown that there is still a statistical advantage (6) and scatter correction methods have been shown to be quite accurate (7,8). The ECAT EXACT3D (model 966; CTI/Siemens, Knoxville, TN) is a 3D-only tomograph with a large axial field of view (FOV) and high spatial and temporal resolution (8). Six rings of  $Bi_4Ge_3O_{12}$  detector blocks (ECAT EXACT HR+) (9) are mounted on a gantry with a diameter of 83 cm and an axial FOV of 23.4 cm. The block detectors are organized into cassettes (buckets), each containing 12 blocks (6 axially, 2 radially).

The aim of this study was to test the hypothesis that absolute quantification of regional full-wall-thickness MBF, transmural MBF, is feasible and accurate using a 3D-only PET tomograph. Therefore, in anesthetized pigs, we com-

Received May 23, 2001; revision accepted Dec. 3, 2001.  
For correspondence or reprints contact: Ornella Rimoldi, MD, Medical Research Council Clinical Sciences Centre, Hammersmith Hospital, Du Cane Rd., London W12 0NN, United Kingdom.  
E-mail: ornella.rimoldi@csc.mrc.ac.uk

pared the measurement of MBF obtained by means of the ECAT EXACT3D camera and  $\text{H}_2^{15}\text{O}$  with that obtained using the radioactive microsphere method as the gold standard over a wide flow range.

## MATERIALS AND METHODS

### Animal Preparation and Surgery

The principles of laboratory animal care and use in accordance with the Animals (Scientific Procedures) Act of 1986 were followed. After a 12-h fast, 9 large white pigs ( $35 \pm 4$  kg) were premedicated with intramuscular azaperone ( $2 \text{ mg} \cdot \text{kg}^{-1}$ ). Anesthesia was induced with thiopentone ( $25 \text{ mg} \cdot \text{kg}^{-1}$ ) and maintained with propofol infusion ( $9\text{--}20 \text{ mg} \cdot \text{kg}^{-1} \cdot \text{h}^{-1}$ ). The animals were artificially ventilated ( $15 \text{ mL} \cdot \text{min}^{-1} \cdot \text{kg}^{-1}$ ) with room air and supplemented with oxygen, as required, to maintain blood partial pressure of  $\text{O}_2$ , partial pressure of  $\text{CO}_2$ , and pH within physiologic limits.

Teflon catheters (DuPont, Wilmington, DE) were implanted in the femoral artery and vein, through an incision in the groin, to measure aortic pressure, sample blood, and administer radioactive tracers. The heart was exposed through an incision in the fourth left intercostal space. A solid-state pressure gauge (Konigsberg Instruments, Pasadena, CA) was inserted into the left ventricle (LV). The circumflex ( $n = 4$ ) or the left anterior descending ( $n = 5$ ) coronary arteries were dissected 2 cm from their origin, and a transit time flow meter (Triton Technology, San Diego, CA) and a hydraulic occluder were implanted. Ultrasonic crystals (Triton Technology) were placed into the inner third of the LV wall in the center of the area to be subtended by the stenosed artery to monitor circumferential fiber shortening. A catheter was inserted in the left atrial appendage for radioactive microsphere injection. The chest was then closed in layers after restoring negative pressure.

Mean arterial, LV peak systolic, and end-diastolic pressures, LV  $\text{dP/dt}$  (first derivative of LV pressure with respect to time, to assess LV contractility), segmental shortening, coronary blood flow, and 3 electrocardiograph leads were continuously monitored and recorded on a multichannel recorder (DISS, Pinckney, MI). Average values for individual parameters were calculated from digitized data sampled at the time of PET data acquisition.

### Experimental Protocol

After baseline hemodynamic measurements, the occluder was inflated slowly through a motor-driven syringe to reduce mean coronary blood flow by  $\sim 50\%$ . Once the desired flow rate was achieved, flow was kept stable by adjusting the pressure in the hydraulic occluder for the duration of the 2 PET  $\text{H}_2^{15}\text{O}$  acquisitions (i.e., under resting and stress [dipyridamole] conditions). MBF was also measured using  $15\text{-}\mu\text{m}$  plastic microspheres labeled with either  $^{57}\text{Co}$  (rest) or  $^{46}\text{Sc}$  (stress) to high specific radioactivity (NEN Research Products, Boston, MA). The microspheres were suspended in 10% dextran. To ensure a homogeneous suspension for injection, each vial was spun in a vortex until the microspheres were mixed in the solution. Finally, before injection, microspheres were sonicated in warm water ( $\sim 40^\circ\text{C}$ ) for 15–30 min. Approximately  $1.6 \times 10^6$  microspheres ( $0.5\text{--}2.5 \text{ MBq}$  in  $0.5\text{--}1.5 \text{ mL}$ ) were injected into the left atrium over 4 s. A reference blood sample was withdrawn from the femoral artery over 2 min at a rate of  $7.5 \text{ mL} \cdot \text{min}^{-1}$ , starting 10 s before the injection of microspheres.

### PET Scanning

Scanning was performed with an ECAT EXACT3D (8). The acquisition system of this scanner has a flexible design that can record data in frame and list mode. List-mode acquisition was used in this study because it represents a significant feature of the tomograph, allowing efficiency of data storage and high temporal sampling with flexible frame rebinning posthoc. Emission scanning was performed with an energy window of 350–650 keV. Transmission scanning was performed with a single photon point source ( $150 \text{ MBq } ^{137}\text{Cs}$ ;  $\gamma$ -energy, 0.663 MeV; half-life, 30.2 y) contained in a small pellet that was driven in a fluid-filled steel tube wound into a helix and positioned just inside the detector ring (6,10).

Animals were positioned in the scanner lying on their right side, and a transmission scan was recorded for 10 min. To image the blood pool,  $\text{C}^{15}\text{O}$  ( $1.5 \text{ MBq} \cdot \text{mL}^{-1}$ ) was administered through the endotracheal tube for 4 min at a rate of  $500 \text{ mL} \cdot \text{min}^{-1}$ . A list-mode PET scan and serial blood sampling (3 mL arterial blood every minute) started at the end of  $\text{C}^{15}\text{O}$  inhalation and lasted for 18 min.

Subsequently, MBF was measured using  $\text{H}_2^{15}\text{O}$  ( $110 \text{ MBq}$ ) injected intravenously over 20 s at an infusion rate of  $10 \text{ mL} \cdot \text{min}^{-1}$ . During the 2 PET MBF measurements, radioactive microspheres were injected 40 s after the start of  $\text{H}_2^{15}\text{O}$  infusion. The total duration of the  $\text{H}_2^{15}\text{O}$  scan was 10 min. It is important to note that after the administration of  $\text{C}^{15}\text{O}$  and  $\text{H}_2^{15}\text{O}$ , list-mode scan data were collected for extended periods to optimize the start of framing relative to the arrival of radioactivity in the FOV and to allow for the possible lengthening of the framing period. This use of what was designated previously as the decay period did not affect the total duration of the study and resulted in a negligible increase in the amount of disk space required. MBF was measured twice in each animal: at baseline with the occluder inflated and after administration of dipyridamole ( $0.56 \text{ mg} \cdot \text{kg}^{-1}$ ) infused intravenously over 4 min. During dipyridamole-induced hyperemia, the delivery of  $\text{H}_2^{15}\text{O}$  was timed to start at 5 min from the beginning of dipyridamole infusion. A second  $\text{C}^{15}\text{O}$  scan was repeated after the second  $\text{H}_2^{15}\text{O}$  scan ( $n = 7$ ).

### PET Data Analysis

All emission data were acquired in list mode and then sorted into sinogram data off-line on an Ultra 10 workstation (Sun Microsystems, Mountain View, CA). For each list-mode dataset, a total counting rate curve was generated. This curve defines the global tomograph response to the arrival and passage of radioactivity through the FOV and was used to define the frame durations into which the list-mode data were rebinned. The maximum ring difference used was 40 (acceptance angle,  $\pm 13.6^\circ$ ), with a span of 9, which results in 559 sinograms per frame, each the sum of 4 or 5 adjacent individual sinograms except for those at the edge of the FOV. Averaging of 2 adjacent views in the sinogram (i.e., mashing) was performed to further reduce data volumes. This process causes only a very slight loss of transaxial resolution (8). Each sinogram consists of 288 projection bins  $\times$  144 projection views. The total frame size is 46.4 MB.

Each of the  $\text{H}_2^{15}\text{O}$  list-mode acquisitions was sorted into 27 frames, a background frame, followed by a 20-s frame to allow for the circulation of the activity, followed by  $14 \times 5\text{-s}$ ,  $3 \times 10\text{-s}$ ,  $4 \times 20\text{-s}$ , and  $4 \times 30\text{-s}$  frames to accurately describe the kinetics of the radioactive water in the body. The background frame had a variable length from the start of acquisition to the arrival of activity in

the FOV, minus 20 s. The arrival time of the activity in the FOV was determined from the total counting rate curve.

A static  $C^{15}O$  emission image was generated after the integration of the list-mode data for a period of 480 s. The start time for the integration occurred either at 1 min after the end of the  $C^{15}O$  inhalation, thus allowing for a period of equilibration of radioactivity within the cardiovascular system, or, if occurring later, at 10 s after the point at which true coincidence counts began to fall after saturation on those occasions when the early accumulation of scan data was counting-rate limited in the acquisition hardware.

**Data Corrections and Reconstruction.** All data were normalized by correcting for geometric effects, individual crystal efficiencies, and plane-to-plane calibration, obtained from separate scans of a rotating rod source and a uniform cylinder (8).

A model-based scatter correction method was used, available in the standard software supplied by the tomograph manufacturer (11). This method iteratively calculates the scatter distribution in the projection from raw emission and transmission data. We have reported that the error due to scattered photons is <5% in different thoracic regions of a European Commission chest phantom after applying the correction method (8).

The main limitation of the scanner is the counting rate saturation of the real time sorter, which, for a maximum ring difference of 40, occurs close to  $2.9 \times 10^6$  total coincidences (prompts + randoms) per second. This leads to a limit on total activity within the coincidence FOV of  $\sim 80$  MBq ( $11 \text{ kBq} \cdot \text{mL}^{-1}$  in a 20-cm cylinder). The error in dead-time correction, which has been quantified in phantom experiments, is a maximum of 3% at the saturation activity (8).

Transmission data were reconstructed using single slice rebinning (12). The transmission images, by means of a local threshold technique (6,13), were segmented into low- and high-attenuating media (lung and soft tissue) regions. Pixels in each segment were scaled to the theoretic  $\mu$  values of  $0.032$  and  $0.095 \text{ cm}^{-1}$ , respectively (13). The histogram peaks of the attenuation coefficient ( $\mu$  values) were reassigned to those appropriate for narrow-beam attenuation at 511 keV, and the resulting data were then forward projected to form the required attenuation correction files.

The emission data were reconstructed with the reprojection algorithm (14,15) applying a transaxial Hanning filter (cutoff, 0.5 cycle/pixel) and a zoom factor of 2.29. This resulted in a dataset containing 95 planes of size  $128 \times 128$  with a measured voxel size of  $2.29 \times 2.29$  (transaxial)  $\times 2.43$  (axial)  $\text{mm}^3$ . The transaxial resolution full width at half maximum (FWHM) was  $6.7 \pm 0.1$  mm in the center of the FOV and  $7.8 \pm 0.1$  mm (radial) and  $6.9 \pm 0.1$  mm (tangential) at 10-cm offset (8). Additionally, the  $H_2^{15}O$  image data were rebinned into 2D sinograms using a Fourier rebinning (FORE) algorithm (16).

All images and 2D sinograms were transferred to an Ultra 10 workstation and analyzed with dedicated software running in the MATLAB programming language (The MathWorks Inc., Natick, MA).

**Vascular Image.** A blood volume ( $[V_B] \text{ mL}_{\text{BLOOD}} \cdot \text{mL}_{\text{ROI}}^{-1}$ , where ROI = region of interest) image was obtained from the static  $C^{15}O$  image ( $\text{kBq} \cdot \text{mL}_{\text{ROI}}^{-1}$ ). Because of a progressive fall in the decay-corrected concentration of  $C^{15}O$  in blood with time (possibly caused by incomplete mixing in the vascular pool or an increased CO elimination rate in this experimental model), the single-frame  $C^{15}O$  image was converted to a regional distribution of blood volume in the classical manner by dividing the image counts, voxel by voxel, by the integral of radioactivity in the

sampled arterial blood ( $\text{kBq} \cdot \text{mL}_{\text{BLOOD}}^{-1}$ ). This integration, which was performed over the list-mode scan-data integration period, was facilitated by fitting the radioactivity–time curve (decay corrected to time of sampling) to an exponential function. The extravascular tissue volume ( $[V_{EV}] \text{ mL}_{\text{anatomic tissue}} \cdot \text{mL}_{\text{ROI}}^{-1}$ ) image was derived by subtracting the blood volume image from the normalized transmission image. This parameter is denoted by the term “anatomic tissue fraction” (ATF) (17).

**Myocardial Factor Images and MBF Calculation.** Myocardial images were generated directly from the dynamic  $H_2^{15}O$  scans using a factor analysis technique (18). The main goal was to provide vascular and extravascular myocardial images from the dynamic  $H_2^{15}O$  scan that had an optimal signal-to-noise ratio to be suitable for ROI definition. Briefly, factor sinograms were generated by means of linear dimension reduction of the dynamic FORE sinograms (16). The procedure for the creation of the factor sinograms requires estimates of vascular (right and left heart) and myocardial tissue time–activity curves: the variate and covariate factors. In contrast with the original process, in which lung regions were drawn manually to provide all 3 time–activity curves (18), cluster analysis was applied to the dynamic FORE images to automate and optimize this step. Cluster analysis was used to segment the dynamic data to identify regions with similar time–activity curves (19). Three clusters were chosen, representing mixed venous (right ventricular [RV] chamber), arterial (left atrium and LV chamber), and myocardial tissue regions. For each cluster, a probability matrix (cluster image: Figs. 1A–C) was generated together with the associated time–activity curves (Fig. 1, right). A cluster image thus represents a set of regional probability values that describe the degree of association of a given voxel with the cluster time–activity curves. The resulting 3 cluster time–activity curves were subsequently entered into the factor analysis to provide the 2 factor sinograms. Factor images describing tissue and blood distributions were generated by iterative reconstruction (Fig. 2) (18).

Factor images were resliced into 5-mm-thick short-axis images (voxel size,  $1.12 \times 1.12 \times 5.0 \text{ mm}^3$ ) in an orientation perpendicular to the long axis of the LV. This transformation matrix was also used to reslice all transaxial images, including the dynamic water images and the blood volume images.

Starting from the apex, 12 consecutive short-axis planes (each 2 planes corresponding to 1 slice of the anatomic sections of the heart used for the microsphere analysis) were determined visually for ROI definition. ROIs were placed manually on the factor images by defining the inner and outer LV wall and radially dividing the myocardium into 4 segments for the apical planes and 6 segments for the middle and basal planes. The anterior interventricular groove, the point identifying the meridian plane of the anatomic cut, was defined as the separation line between septal and anterior regions. All segments were then grouped into 16 anatomic regions and projected onto the dynamic 3D water image to extract tissue time–activity curves.

Small circular ROIs ( $\sim 60$  voxels; radius, 5 mm each) were placed in the left atrium on as many consecutive planes as possible (3–6 planes) to obtain the arterial input function. Similarly, a mixed venous blood time–activity curve was defined by placing ROIs in the RV cavity. A global blood volume recovery factor was then determined for the left atrial region by transposing the left atrial ROIs to the blood volume image determined using  $C^{15}O$ .

Arterial, venous, and tissue time–activity curves were fitted to a single-compartment model to give values of regional and global



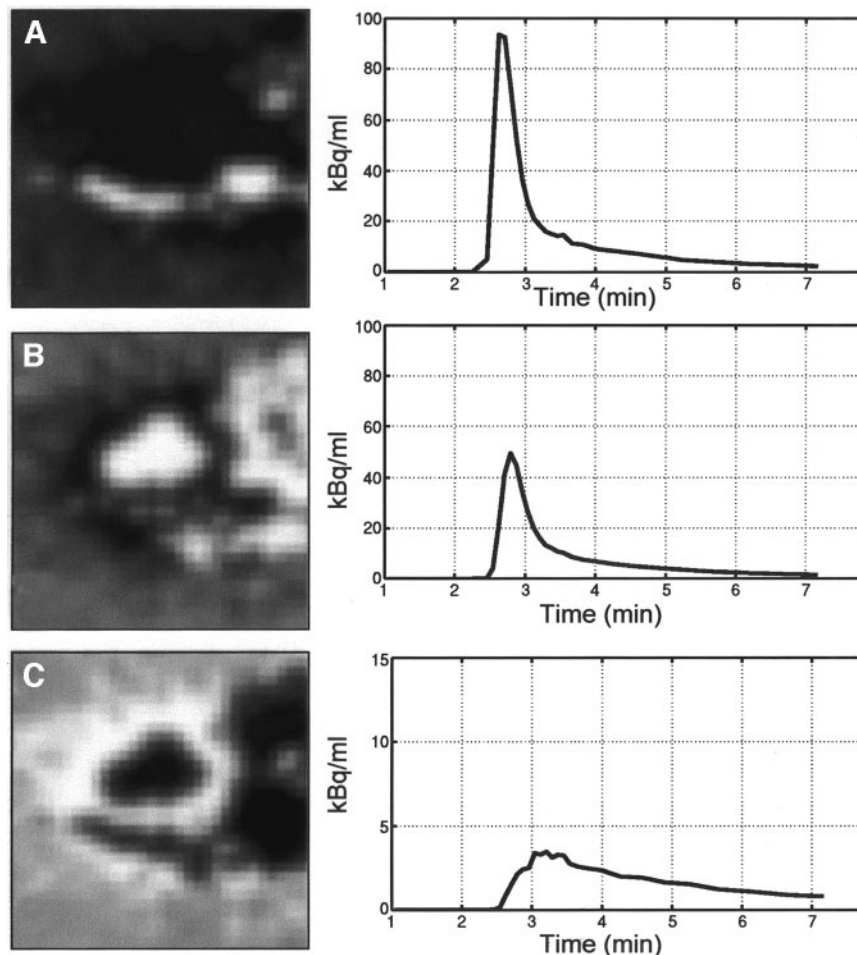


**FIGURE 1.** Cluster probability images of transaxial planes and corresponding time-activity curves. (A) Venous cluster (right ventricular cavity). (B) Arterial cluster (left ventricular cavity). (C) Myocardial tissue cluster.

MBF ( $\text{mL} \cdot \text{L}^{-1} \cdot \text{min}^{-1}$ ) and perfusable tissue fraction ([PTF]  $\text{mL}_{\text{exchangeable tissue}} \cdot \text{mL}_{\text{ROI}}^{-1}$ ) as described (17,20). The PTF-to-ATF ratio, which has previously been termed perfusable tissue index ([PTI]  $\text{mL}_{\text{exchangeable tissue}} \cdot \text{mL}_{\text{anatomic tissue}}^{-1}$ ), represents the proportion of extravascular tissue perfusable by  $\text{H}_2^{15}\text{O}$ . For comparison with microsphere flow data, MBF PET results were di-

vided by the density of myocardial tissue ( $1.04 \text{ g} \cdot \text{mL}^{-1}$ ) to express MBF in  $\text{mL} \cdot \text{g}^{-1} \cdot \text{min}^{-1}$ .

#### Calculation of MBF with Radiolabeled Microspheres

After PET scanning, the pigs were killed with an overdose of barbiturates. The heart was excised and cut into 6 or seven 10-

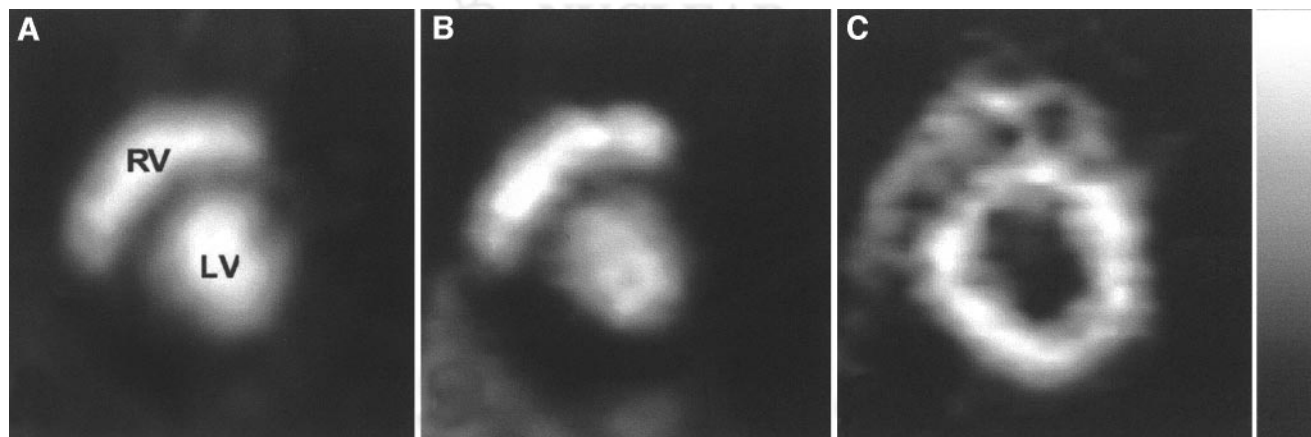


**FIGURE 2.** Short-axis images obtained from representative study show blood pool (A) measured with  $\text{C}^{15}\text{O}$ , which labels erythrocytes through formation of carboxyhemoglobin, and distribution of  $\text{H}_2^{15}\text{O}$  separated in blood (B) and myocardial tissue (C) component. B and C are calculated by means of factor analysis. RV = right ventricle; LV = left ventricle.

mm-thick slices perpendicular to the long axis of the LV. Each slice was further cut into 8 equally sized wedges using the inter-ventricular groove as a marker point for the meridian cut between the anterior and septal region. Tissue and arterial blood samples were counted in an automated  $\gamma$ -counter (CompuGamma 1282; Wallac Oy, Turku, Finland), and blood flow per gram of myocardium was calculated by dividing the sample radioactivity by sample weight using a standard reference technique (21). To allow comparison with regional PET flow values (22), microsphere MBF data were grouped into 16 standard regions (anterior, lateral, posterior, and septum for the apex; anterior, lateral, inferior, posterior, posterior septum, and inferior septum for the middle and the base of the heart).

### Statistics

Results are expressed as mean  $\pm$  SD. Hemodynamic measurements, PTF and PTI, were compared by means of ANOVA and post hoc Fisher protected least-significant difference test. The 2 series, PET and microsphere MBF and their difference, were tested for homoscedasticity by means of the F test for equality of variances. Linear least-square regression was performed with microsphere MBF as the independent variable against PET MBF to test the deviation from the line of identity. The mean difference and the average between paired measurements (microsphere and PET MBF) were calculated to test the agreement between the 2 measurements according to Bland and Altman (23). A value of  $P < 0.05$  was considered statistically significant.

## RESULTS

### Hemodynamics

The baseline hemodynamic variables and their changes are given in Table 1. Coronary blood flow and segmental shortening were reduced by  $\sim 50\%$  in the ischemic area without significant changes in systemic blood pressure or global LV contractility (LV dP/dt). The systemic vasodilation induced by dipyridamole significantly reduced aortic systolic and diastolic blood pressure. The flow in the constricted coronary artery was slightly but not significantly increased, as expected, after dipyridamole infusion.

### Image Analysis

Representative short-axis factor images of blood pool and myocardium from 1 study are shown in Figures 2B and 2C. The factor images are of excellent quality, and the factor images of the blood pool compare well with the correspond-

ing blood-pool images obtained after inhalation of  $C^{15}O$  (Fig. 2A).

### Left Atrial Blood Volume Recovery Factors

One baseline blood volume measurement was unobtainable because of a failure in the data transfer of the associated transmission scan. Left atrial recovery values for the remaining 8 studies were found to be high ( $0.84 \pm 0.06 \text{ mL}_{\text{BLOOD}} \cdot \text{mL}_{\text{ROI}}^{-1}$ ). However, the interstudy variation in recovery factors (range,  $0.78\text{--}0.92 \text{ mL}_{\text{BLOOD}} \cdot \text{mL}_{\text{ROI}}^{-1}$ ) was substantially greater than the differences obtained for the repeated measurements made in 6 studies (typically 3%; arithmetic mean,  $-0.8\%$ ; range,  $-6.6\%$  to  $3.6\%$ ).

### MBF, PTF, and PTI

A total of 256 paired microsphere and PET measurements were obtained in 8 pigs, with microsphere flows ranging from  $0.05$  to  $4.40 \text{ mL} \cdot \text{g}^{-1} \cdot \text{min}^{-1}$ . Three scans were excluded from the direct comparison because of technical delays between the PET image acquisition and the injection of microspheres. In 1 pig, an additional hyperemic scan obtained during intravenous adenosine infusion ( $140 \text{ mg} \cdot \text{kg}^{-1} \cdot \text{min}^{-1}$ ) was included in the comparison.

The F test performed on the 2 series of measurements showed equality of variances. The slope of the scatter diagram in Figure 3A ( $y = 0.15 + 0.97x$ ;  $r = 0.87$ ;  $r^2 = 0.76$ ) was close to unity and the intercept was close to zero, thus indicating good correlation between the gold standard microsphere MBF and PET MBF over a broad range of values. The Bland-Altman plot of the differences between the 2 measurements against the average value is shown in Figure 3B. The mean difference between microsphere and PET MBF was  $-0.11 \pm 0.36 \text{ mL} \cdot \text{g}^{-1} \cdot \text{min}^{-1}$  with 95% of the differences lying between the limits of agreement of  $-0.83$  and  $0.61 \text{ mL} \cdot \text{g}^{-1} \cdot \text{min}^{-1}$ .

The best agreement between the 2 methods was observed under resting conditions (Fig. 4A) with a mean difference of  $-0.09 \pm 0.22 \text{ mL} \cdot \text{g}^{-1} \cdot \text{min}^{-1}$  and limits of agreement of  $-0.53$  and  $0.35 \text{ mL} \cdot \text{g}^{-1} \cdot \text{min}^{-1}$ . During hyperemia, in spite of a similar difference of  $-0.13 \pm 0.45 \text{ mL} \cdot \text{g}^{-1} \cdot \text{min}^{-1}$ , the limits of agreement were broader:  $-1.03$  and  $0.77 \text{ mL} \cdot \text{g}^{-1} \cdot \text{min}^{-1}$  (Fig. 4B). The agreement between microsphere and PET MBF in the 2 different ischemic

TABLE 1

Hemodynamic Parameters at Baseline After Inflation of Hydraulic Occluder (Ischemia) and During Dipyridamole Infusion

	Systolic pressure (mm Hg)	Diastolic pressure (mm Hg)	Heart rate (beats/min)	End-diastolic LV pressure (mm Hg)	LV dP/dt maximum (mm Hg/s)	% Segment shortening	Mean coronary blood flow (mL/min)
Baseline	$113 \pm 18$	$74 \pm 15$	$94 \pm 20$	$9 \pm 3$	$1,599 \pm 319$	$18.16 \pm 3.8$	$33 \pm 13$
Ischemia	$111 \pm 12$	$74 \pm 12$	$106 \pm 17$	$9 \pm 4$	$1,373 \pm 295$	$8.15 \pm 2.9^*$	$16 \pm 10^*$
Ischemia + dipyridamole	$72 \pm 8^{\dagger}$	$38 \pm 6^{\dagger}$	$110 \pm 13$	$8 \pm 4$	$1,208 \pm 309$	$9.1 \pm 3.2^*$	$27 \pm 12$

\*Significantly different from baseline ( $P < 0.05$ ).

$\dagger$ Ischemia significantly different from ischemia + dipyridamole.

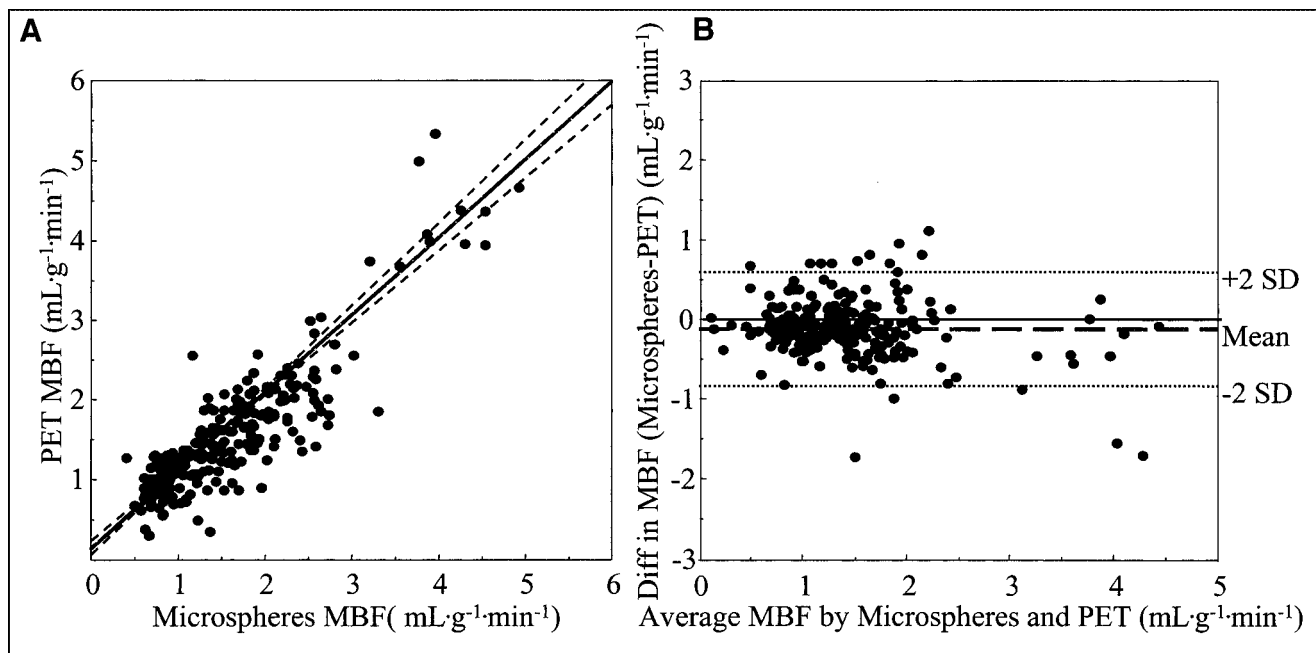


**FIGURE 3.** Regression analysis (A) and Bland-Altman plot (B) of variation of MBF obtained from microspheres and PET in all ROIs. Dashed lines = 95% confidence limits for slope; Diff = difference.

territories during hyperemia appeared to be more precise in the circumflex coronary artery (mean difference,  $-0.04 \pm 0.39 \text{ mL} \cdot \text{g}^{-1} \cdot \text{min}^{-1}$ ; limits of agreement,  $-0.82$  and  $0.74 \text{ mL} \cdot \text{g}^{-1} \cdot \text{min}^{-1}$ ; SE, 0.08) (Fig. 5A) than in the left anterior descending coronary artery territory (mean difference,  $-0.15 \pm 0.53 \text{ mL} \cdot \text{g}^{-1} \cdot \text{min}^{-1}$ ; limits of agreement,  $-1.21$  and  $0.91 \text{ mL} \cdot \text{g}^{-1} \cdot \text{min}^{-1}$ ; SE, 0.094) (Fig. 5B), even though no significant difference was detected.

Table 2 summarizes the comparison of the accuracy of the measurement of MBF in the various regions of the LV. The apical and posterior regions show a greater variance in the differences between PET and microsphere measurements.

The values of PTF and PTI in control and ischemic tissue at rest (PTF in  $\text{mL}_{\text{exchangeable tissue}} \cdot \text{mL}_{\text{ROI}}^{-1}$ : control,  $0.66 \pm 0.10$ ; ischemic,  $0.66 \pm 0.11$ ; PTI in  $\text{mL}_{\text{exchangeable tissue}} \cdot \text{mL}_{\text{anatomic tissue}}^{-1}$ : control,  $0.93 \pm 0.13$ ; ischemic,  $0.94 \pm 0.12$ ) and during dipyridamole-induced hyperemia (PTF in  $\text{mL}_{\text{exchangeable tissue}} \cdot \text{mL}_{\text{ROI}}^{-1}$ : control,  $0.69 \pm 0.10$ ; ischemic,  $0.59 \pm 0.15$ ; PTI in  $\text{mL}_{\text{exchangeable tissue}} \cdot \text{mL}_{\text{anatomic tissue}}^{-1}$ : control,  $0.95 \pm 0.17$ ; ischemic,  $0.83 \pm 0.20$ ) are illustrated in Figure 6. It is worth noting that PTF and PTI are reduced significantly during hyperemia in the territories subtended by the stenotic coronary arteries.

## DISCUSSION

In this study, measurements of MBF in absolute units obtained by 3D PET using  $\text{H}_2^{15}\text{O}$  have been compared with those obtained simultaneously with radiolabeled microspheres. The 2 methods show good correlation over a wide flow range. This is particularly important because, to our knowledge, a 3D PET

acquisition technique for the absolute quantification of MBF with  $\text{H}_2^{15}\text{O}$  has not been reported previously.

One of the greatest improvements in the analysis of  $\text{H}_2^{15}\text{O}$  scans has been the development of a method for the generation of factor images directly from the dynamic  $\text{H}_2^{15}\text{O}$  scans (18). The high quality of the myocardial and blood-pool images (Fig. 2) overcomes the need for an additional  $\text{C}^{15}\text{O}$  scan, for blood volume quantification, and greatly simplifies the PET protocol in addition to reducing the radiation dose to the patient. The generation of factor images requires the input of 2D sinograms. This is still a limitation because all 3D raw data have to be transformed into 2D sinograms using a FORE rebinning technique (16), which enlarges the required disk space because of the need for 3D and 2D sinograms. A time-activity curve obtained from a lung region was used previously to represent the LV and RV time-activity curves, each being generated by shifting the lung curve to earlier or later times (18). The LV and RV time-activity curves together with a normal tissue kinetic curve, generated using a standard single-compartment model with MBF set to  $1 \text{ mL} \cdot \text{min}^{-1} \cdot \text{mL}^{-1}$ , were then used in the factor analysis to separate myocardial and blood components within the sinograms (18). In this study, the use of lung ROIs to derive LV and RV time-activity curves was replaced by a cluster analysis approach that automatically generates 3 different characteristic dynamic curves from the dynamic images (Fig. 1) (19). This represents an appreciable improvement toward observer independence because the factor imaging can be fully automated.

The administration procedure has been shown to influence the accuracy of the results (24). Different  $\text{H}_2^{15}\text{O}$  ad-

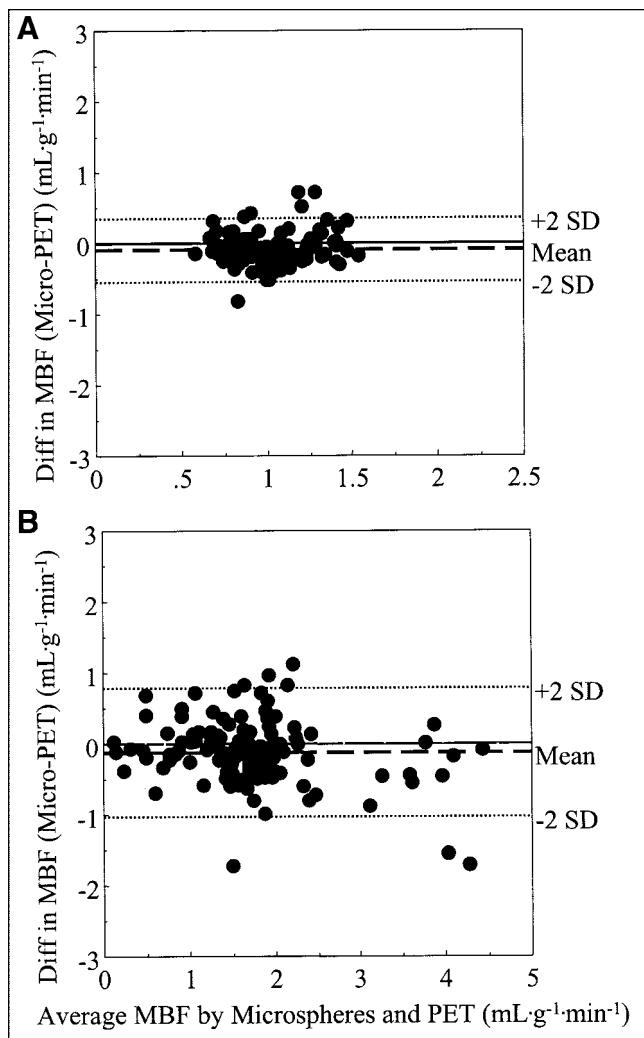


**FIGURE 4.** Bland–Altman plots show agreement of MBF obtained from microspheres and PET under resting conditions (A) and during hyperemia induced with dipyridamole (B). Diff = difference.

ministration protocols have been proposed in the past to measure MBF, including bolus injection (25–27), slow infusion (28), and inhalation of C<sup>15</sup>O<sub>2</sub> (29). In a direct comparison of different administration protocols, Iida et al. (24) and Hermansen et al. (20) showed that bolus injection provides the most accurate method with the smallest inter-subject and interregional variation. Accordingly, in this study we have used a bolus injection technique delivered automatically over 20 s. Because of the relatively sharp signal that is generated by a bolus injection, the total radioactivity dose given to the animals had to be limited in order not to saturate the counting rate of the scanner.

We aimed to compare PET MBF with microsphere MBF within relatively small regions (16 segments per whole LV), matching the territories of distribution of the main coronary arteries to validate MBF measurements. We applied a standard regional analysis method that is used routinely in human studies for the analysis of MBF and viability (20).

Validation of regional MBF quantification using PET with H<sub>2</sub><sup>15</sup>O (C<sup>15</sup>O<sub>2</sub> inhalation) has been performed in our institution (29) using larger, homogeneous nonischemic ROIs in a canine model. In that study, the 2D PET camera (ECAT 931–08/12; CTI/Siemens) used for the acquisition of dynamic PET data had an inferior sensitivity and spatial resolution (about 9 mm FWHM, transaxial) compared with that of the ECAT EXACT3D. Overall, Araujo et al. (29) obtained a good correlation between MBF measured with microspheres and PET. Similar to this study, they observed a larger scatter at high flows. The comparability of the results adds experimental evidence to mathematic simulations that show a lower precision of the H<sub>2</sub><sup>15</sup>O model at high flow. Another validation study was performed by Bol et al.

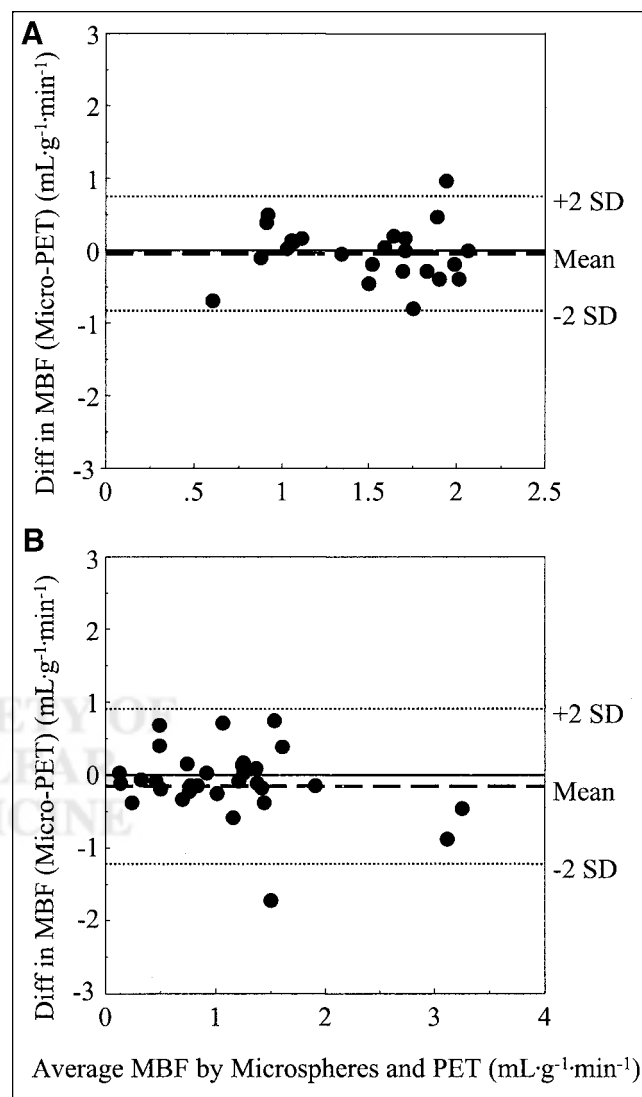


**FIGURE 5.** Bland–Altman plots show agreement of MBF obtained from microspheres and PET during hyperemia induced with dipyridamole. Data are presented for group in which left circumflex coronary artery was occluded (A) and for group in which left anterior descending coronary artery was occluded (B). Diff = difference.



**TABLE 2**

Comparison of Variance of Difference of MBF Measurement Between Microspheres and PET in Different Regions of Left Ventricle

	Basal	Midventricular	Apex
<b>Rest</b>			
Anterior	0.005	0.038	0.126 b*
Lateral	0.012	0.031	0.113 b*
Septal	0.008	0.010	0.032
Posterior	0.124 a, s, i†	0.137 s†	
Inferior	0.007	0.034	0.032
<b>Hyperemia</b>			
Anterior	0.116	0.362 l†	0.254
Lateral	0.063	0.033	0.173 m*
Septal	0.121	0.089	0.096
Posterior	0.135	0.579 l, s†	
Inferior	0.079	0.172 l†	0.200

\*Apical regions significantly different from basal (b) or midventricular (m) regions ( $P < 0.05$ ).

†Significant contrast difference vs. other regions in short-axis partition: a = anterior, l = lateral, s = septal, i = inferior ( $P < 0.05$ ).

(30) using a canine model of acute ischemia, in which MBF was measured with PET using  $H_2^{15}O$  and  $^{13}NH_3$  against radioactive microspheres. They obtained a good correlation between microsphere and PET MBF for both tracers in relatively small ROIs. It is worth noting that Bol et al. obtained the PET data using a single-slice scanner. The large FOV (23.4 cm axially) of the ECAT EXACT3D enables MBF measurements to be made in the whole of the LV as well as time-activity curves in the left atrium. The mean difference between microsphere and PET MBF estimates in this study ( $-0.11 \text{ mL} \cdot \text{g}^{-1} \cdot \text{min}^{-1}$ ) is smaller than that obtained by Bol et al. ( $0.26 \text{ mL} \cdot \text{g}^{-1} \cdot \text{min}^{-1}$ ), whereas the random variability is similar ( $SD = 0.37$  in our study and  $0.38$  in the study of Bol et al.). This is a favorable comparison considering that a factor of 5 times less radioactivity was delivered in this study because of the higher sensitivity of the ECAT EXACT3D scanner. Furthermore, the animals in the study of Bol et al. were smaller on average (with correspondingly less attenuation and scattered radiation). A contributory factor to the small systematic difference seen between PET and microsphere MBF could be related to the value of the recovery coefficients obtained for the left atrial ROIs ( $0.84 \pm 0.06 \cdot \text{mL}_{\text{BLOOD}} \cdot \text{mL}_{\text{ROI}}^{-1}$ ). Recovery values of less than unity would be expected from ungated measurements made on an animal with a heart smaller than that of a human when images are reconstructed with a spatial resolution of 7 mm FWHM. Although no effect on MBF would be expected from a reduction in the magnitude of the arterial input function per se, because MBF is derived from the clearance term in the convolution equation, any significant degree of spillover from tissue regions would be expected to result in an overestimation of MBF. A left atrial ROI was chosen in preference to a

ventricular region to minimize this effect, although previous investigators have shown a small overestimation in MBF when using the left atrium (31).

The scatter on the plots between microsphere and PET MBF could be ascribed to several causes. There are factors inherent in the physical characteristics of the 2 tracers.  $H_2^{15}O$  is freely diffusible and the resulting MBF represents a mean value determined over a period of 2–3 min. Microspheres are trapped with a first-pass extraction mechanism, which ideally should approximate erythrocyte distribution, and the measurement of MBF is instantaneous (21). These differences have a broader impact at high flows when the excess microsphere deposition in high-flow regions contributes to a biasing of the comparison between the estimates of MBF obtained with these 2 tracers (32). The heterogeneity of regional flows in the myocardium is broad, and the smaller the regions measured, the greater will be the observed dispersion (33). When 2 different techniques are used, as in this study, the likelihood of mismatching between in vivo and ex vivo measurements results in an increased random variability mainly in the apical and posterior regions. A major determinant of spread can be the regional misalignment between the anatomic ex vivo slice used for the microsphere assessment of MBF and the image of the beating heart obtained with PET. To minimize this problem we used, as a reference point, the interventricular groove to segment the planes into 4–6 regions. This is a simple operation in the case of autoradiography, where the position of the interventricular groove can be easily followed. In PET, the detection of the reference point becomes difficult in the apical regions, where the RV is less discernible.

In this study, we show that PTF and PTI are reduced by 10% during hyperemic stress in the ischemic segments, in line with the findings of Iida et al. (34), who showed that a reduction of these variables correlated with the degree of myocardial infarction in a canine model. In our porcine model, characterized by a sparse collateral circulation, the pressure drop across the flow-limiting stenosis that occurs with increased flow could cause a myocardial steal and inhomogeneous distribution of MBF reflected by the changes in PTF and PTI.

The use of the list-mode acquisition in the ECAT EXACT3D provides high (milliseconds) temporal resolution and a more efficient and flexible data storage than the frame-mode acquisition, especially for short-lived tracers, and data can be rebinned off-line. For a standard  $H_2^{15}O$  acquisition of 27 frames, 1 frame-mode scan represents 1.2 GB, whereas the list-mode file (for an infusion of 93 MBq) is less than half this size (8). Despite the unprecedented efficiency of the ECAT EXACT3D, the data were reconstructed with a smoother Hanning filter to improve the image quality. However, the good correlation with microsphere flow, as well as the high recovery factors in the blood volume measurements, indicate that spillover effects did not significantly compromise the results. The high efficiency of



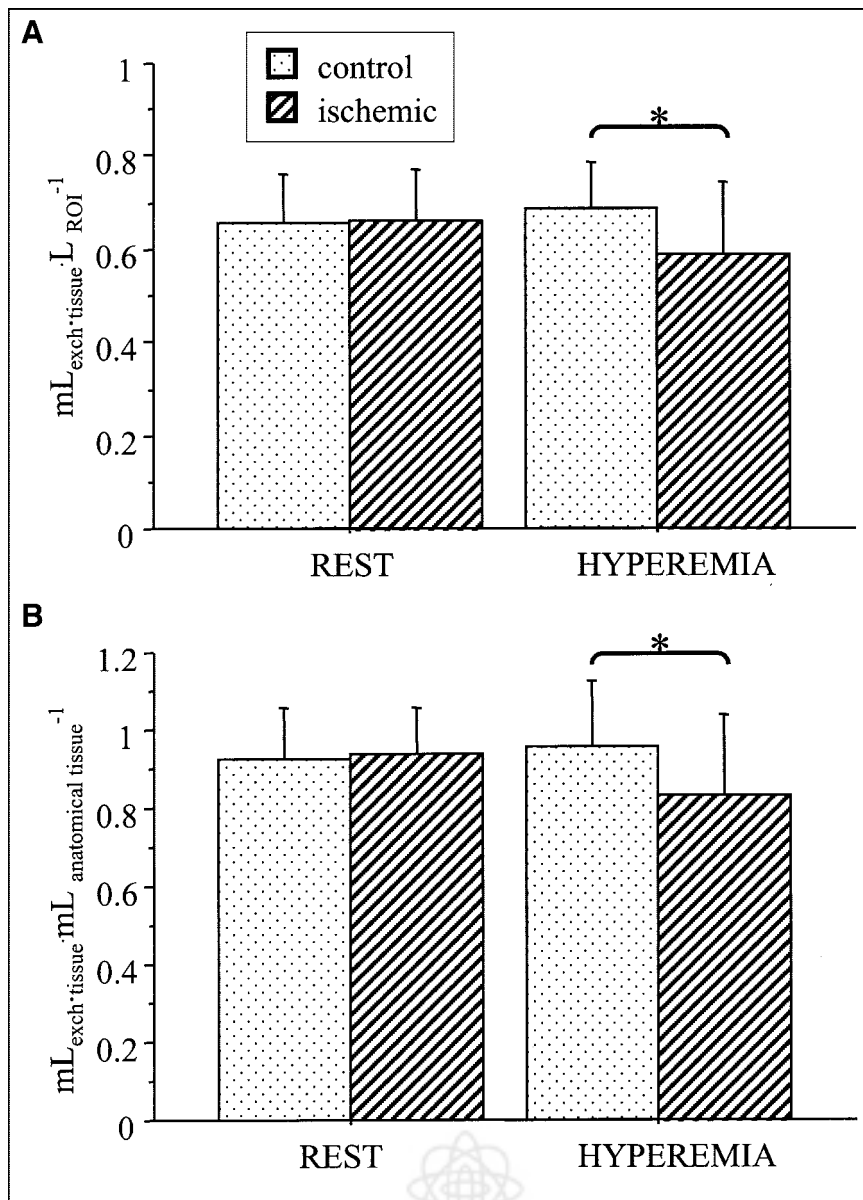


**FIGURE 6.** Histogram shows comparison of PTF (A) and PTI (B) in normally perfused (control) and ischemic myocardium. Values of PTF and PTI are reduced during dipyridamole-induced stress (hyperemia) \* $P < 0.05$ .

the ECAT EXACT3D combined with a higher resolution filter could enable measurement of the transmural distribution of MBF across the LV wall.

## CONCLUSION

The absolute quantification of myocardial blood flow with the ECAT EXACT3D and  $H_2^{15}O$  is feasible and accurate. Three-dimensional acquisition allows reduction of patient radiation dose while maintaining high counting statistics and points the way to future PET research.

## ACKNOWLEDGMENTS

The authors thank Drs. Roger Gunn and Flemming Hermansen for their help on cluster and factor analysis and the staff of the Cyclotron Unit (Imaging Research Solutions Ltd.) for their interest and support, especially the radiogra-

phers for their invaluable technical assistance. This research was supported in part by a grant from the Innovative Medizinische Forschung (grant Sc-1-5-II/96-20) of the University of Münster.

## REFERENCES

1. Kaufmann PA, Gnechi-Ruscione T, Yap JT, Rimoldi O, Camici PG. Assessment of the reproducibility of baseline and hyperemic myocardial blood flow measurements with  $^{15}O$ -labeled water and PET. *J Nucl Med.* 1999;40:1848–1856.
2. Uren NG, Melin JA, De Bruyne B, Wijns W, Baudhuin T, Camici PG. Relation between myocardial blood flow and the severity of coronary artery stenosis. *N Engl J Med.* 1994;330:1782–1788.
3. Czernin J, Barnard RJ, Sun KT, et al. Effect of short-term cardiovascular conditioning and low-fat diet on myocardial blood flow and flow reserve. *Circulation.* 1995;92:197–204.
4. de Silva R, Camici PG. Role of positron emission tomography in the investigation of human coronary circulatory function. *Cardiovasc Res.* 1994;28:1595–1612.
5. Spinks TJ, Jones T, Gilardi MC, Heather JD. Physical performance of the latest

- generation of commercial positron scanner. *IEEE Trans Nucl Sci.* 1988;35:721–725.
6. Bailey DL, Miller MP, Spinks TJ, et al. Experience with fully 3D PET and implications for future high-resolution 3D tomographs. *Phys Med Biol.* 1998;43:777–786.
  7. Watson CC, Newport D, Casey ME, deKemp RA, Beanlands RS, Schmand M. Evaluation of simulation-based scatter correction for 3-D PET cardiac imaging. *IEEE Trans Nucl Sci.* 1997;44:90–97.
  8. Spinks TJ, Jones T, Bloomfield PM, et al. Physical characteristics of the ECAT EXACT3D positron tomograph. *Phys Med Biol.* 2000;45:2601–2618.
  9. Brix G, Zaers J, Adam L-E, et al. Performance evaluation of a whole-body PET scanner using the NEMA protocol. *J Nucl Med.* 1997;38:1614–1623.
  10. Jones WE, Vaigneur K, Young J, Reed JMC, Nahmias C. The architectural impact of single photon transmission measurements on full ring 3-D positron emission tomography. *IEEE Nucl Sci Symp Med Imaging Conf Rec.* 1995;2:1026–1030.
  11. Watson CC, Newport D, Casey ME. Type A single scatter simulation technique for scatter correction in 3D PET. In: Bendriem B, Townsend D, eds. *Three-Dimensional Image Reconstruction in Radiation and Nuclear Medicine.* Dordrecht, The Netherlands: Kluwer Academic; 1998:255–268.
  12. Daube-Witherspoon MG, Muehllehner G. Treatment of axial data in three-dimensional PET. *J Nucl Med.* 1987;28:1717–1724.
  13. Xu M, Luk WK, Cutler PD, Digby WM. Local threshold for segmented attenuation correction of PET imaging of the thorax. *IEEE Trans Nucl Sci.* 1994;41:1532–1537.
  14. Kinahan PE, Rogers JG. Analytic 3-D image reconstruction using all detected events. *IEEE Trans Nucl Sci.* 1988;39:964–968.
  15. Townsend DW, Spinks TJ, Jones T, et al. Three-dimensional reconstruction of PET data from a multi-ring camera. *IEEE Trans Nucl Sci.* 1989;36:1056–1065.
  16. Defrise M, Kinahan PE, Townsend DW, Michel C, Sibomana M, Newport DF. Exact and approximate rebinning algorithms for 3-D PET data. *IEEE Trans Med Imaging.* 1997;16:145–158.
  17. Yamamoto Y, de Silva R, Rhodes CG, et al. A new strategy for the assessment of viable myocardium and regional myocardial blood flow using  $^{15}\text{O}$ -water and dynamic positron emission tomography. *Circulation.* 1992;86:167–178.
  18. Hermansen F, Ashburner J, Spinks TJ, Kooner JS, Camici PG, Lammertsma AA. Generation of myocardial factor images directly from the dynamic oxygen-15-water scan without use of an oxygen-15-carbon monoxide blood-pool scan. *J Nucl Med.* 1998;39:1696–1702.
  19. Ashburner J, Haslam J, Taylor C, Cunningham VJ, Jones T. A cluster analysis approach for the characterization of dynamic PET data. In: Myers R, Cunningham V, Bailey D, Jones T, eds. *Quantification of Brain Function Using PET.* San Diego, CA: Academic Press; 1996:301–306.
  20. Hermansen F, Rosen SD, Fath-Ordoubadi F, et al. Measurement of myocardial blood flow with oxygen-15 labelled water: comparison of different administration protocols. *Eur J Nucl Med.* 1998;25:751–759.
  21. Heymann MA, Payne BD, Hoffman JI, Rudolph AM. Blood flow measurements with radionuclide-labeled particles. *Prog Cardiovasc Dis.* 1977;20:55–79.
  22. Lorenzoni R, Pagano D, Boyd H, Camici PG. A report system for PET assessment of myocardial viability. *Nucl Med Commun.* 1999;20:895–899.
  23. Bland JM, Altman DG. Statistical methods for assessing agreement between two methods of clinical measurement. *Lancet.* 1986;1:307–310.
  24. Iida H, Takahashi A, Tamura Y, Ono Y, Lammertsma AA. Myocardial blood flow: comparison of oxygen-15-water bolus injection, slow infusion and oxygen-15-carbon dioxide slow inhalation. *J Nucl Med.* 1995;36:78–85.
  25. Bergmann SR, Fox KAA, Rand AL, McElvany KD, Welch MJ, Sobel BE. Quantification of regional myocardial blood flow in vivo with  $\text{H}_2^{15}\text{O}$ . *Circulation.* 1984;70:724–733.
  26. Bergman SR, Herrero P, Markham J, Weinheimer CJ, Walsh MN. Noninvasive quantitation of myocardial blood flow in human subjects with oxygen-15-labeled water and positron emission tomography. *J Am Coll Cardiol.* 1989;14:639–652.
  27. Iida H, Kanno I, Takahashi A, et al. Measurement of absolute myocardial blood flow with  $\text{H}_2^{15}\text{O}$  and dynamic positron-emission tomography: strategy for quantification in relation to the partial-volume effect. *Circulation.* 1988;78:104–111.
  28. Huang SC, Schwaiger M, Carson RE, et al. Quantitative measurement of myocardial blood flow with oxygen-15 water and positron computed tomography: an assessment of potential and problems. *J Nucl Med.* 1985;26:616–625.
  29. Araujo LI, Lammertsma AA, Rhodes CG, et al. Noninvasive quantitation of regional myocardial blood flow in coronary artery disease with oxygen-15-labeled carbon dioxide inhalation and positron emission tomography. *Circulation.* 1991;83:875–885.
  30. Bol A, Melin JA, Vanoverschelde JL, et al. Direct comparison of  $^{13}\text{N}$  ammonia and  $^{15}\text{O}$  water estimates of perfusion with quantification of regional blood flow by microspheres. *Circulation.* 1993;87:512–525.
  31. Iida H, Rhodes CG, de Silva R. Use of the left ventricular time-activity curve as a noninvasive input function in dynamic oxygen-15-water positron emission tomography. *J Nucl Med.* 1992;33:1669–1677.
  32. Bassingthwaite JB, Malone MA, Moffett TC, et al. Molecular and particulate depositions for regional myocardial flows in sheep. *Circ Res.* 1990;66:1328–1344.
  33. Bauer WR, Hiller KH, Galuppo P, et al. Fast high-resolution magnetic resonance imaging demonstrates fractality of myocardial perfusion in microscopic dimensions. *Circ Res.* 2001;88:340–346.
  34. Iida H, Tamura Y, Kitamura K, Bloomfield PM, Eberl S, Ono Y. Histochemical correlates of 15-O-water perfusable tissue fraction in experimental canine studies of old myocardial infarction. *J Nucl Med.* 2000;41:1737–1745.

